

# Crustal Structure of the Central African Plateau from Receiver Function Analysis

C.S. Ogden<sup>1,4,\*</sup>, R. Kounoudis<sup>2</sup>, C. Chifwepa<sup>3</sup>, M. Kendall<sup>2</sup>, D. Holwell<sup>1</sup>, S. Fishwick<sup>1</sup>, S.E.J. Nippress<sup>4</sup>, L. Finch<sup>1</sup>, V. Lane<sup>1</sup>, and M.C. Daly<sup>2</sup>

<sup>1</sup>School of Geography, Geology and the Environment, University of Leicester, Leicester, UK

<sup>2</sup>Department of Earth Sciences, University of Oxford, Oxford, UK

<sup>3</sup>Geological Survey Department, Ministry of Mines, Lusaka, Zambia

<sup>4</sup>AWE Blacknest, Brimpton, UK

February 28, 2025

---

\*Corresponding author: Chris Ogden, cogden@blacknest.gov.uk

## Summary

The Central African Plateau records multiple stages of continental extension and assembly between the Congo and Kalahari cratons in south-central Africa. Of significant interest is the formation of the Neoproterozoic Katangan Basin which was subsequently closed during the Pan-African assembly of Gondwana — a region that contains some of the world's largest sediment-hosted copper and cobalt deposits. Whether Katangan Basin development only involved continental extension or progressed to incipient sea-floor spreading is uncertain; so too the extent to which mafic magmatism has modified bulk-crustal structure. Also debated is whether crustal re-working during overprinting by the Pan-African Orogeny to form the Lufilian Arc, was localised or broadly distributed across the entire Katangan Basin. To address these questions, we calculate crustal thickness ( $H$ ) and bulk-crustal  $V_P/V_S$  ratio ( $\kappa$ ) using  $H\text{-}\kappa$  stacking of teleseismic receiver functions recorded by seismograph networks situated across the Central African Plateau, including the new Copper Basin Exploration Science (CuBES) network. Crustal thickness is 45–48 km below the Congo Craton margin, Mesoproterozoic Irumide belt, and Domes region of the Lufilian Arc, 38–42 km below the Bangweulu Craton and 35–40 km below the Pan-African Zambezi Belt in southeastern Zambia. Bulk-crustal  $V_P/V_S$  is generally low (<1.76) across the majority of the Plateau, indicating a dominantly felsic bulk-crustal composition. The formation of the Katangan Basin in the Neoproterozoic is thus unlikely to have been accompanied by voluminous mafic magmatism, significant lower crustal intrusions and/or the formation of oceanic crust. The early-Paleozoic overprinting of the basin by the Pan-African Orogeny, forming the Lufilian Arc, appears to have been most intense in the Domes region, where a deep and highly variable (38–48 km) Moho topography at short length-scales (<100 km), is evident in our  $H\text{-}\kappa$  stacking results. In contrast, shallow and flat Moho architecture with consistently low bulk crustal  $V_P/V_S$  ratios, are observed further south. This flat region includes the Mwembeshi Shear Zone, which is also not associated with a  $V_P/V_S$  ratio contrast, suggesting the fault likely separates two very similar crustal domains.

## Keywords

Africa, Crustal imaging, Moho depth, Crustal structure, Composition and structure of the continental crust, Continental crust

# 1 Introduction

The Central African Plateau (~1.2 km elevation) records the development of several tectonic episodes, from the repeated suturing and break-up of Proterozoic orogenic belts and Cratonic cores, to rifting in Permo-Triassic and Quaternary times (e.g., [Daly et al., 2020](#); [Porada and Berhorst, 2000](#)). Comprising the majority of the Plateau are the Lufilian and Zambezi Belts (Figure 1A), regions which once marked a network of Neoproterozoic basins — most notably the Katangan Basin — that closed during the Pan-African assembly of Gondwana, during the convergence between the Kalahari and Congo Cratons. The geodynamic evolution of the Katangan Basin and subsequent overprinting by the Pan-African Orogeny is debated. Most studies propose a continental rift setting for Katangan Basin formation (e.g., [Unrug, 1983](#); [Porada, 1989](#); [Hanson et al., 1994](#)), however, whether continental rifting progressed to incipient sea-floor spreading, forming new oceanic crust (e.g., [Kampunzu and Cailteux, 1999](#)), is uncertain; so too whether a large igneous province, akin to the Cenozoic-to-recent Ethiopian traps, concurrently developed within the region (e.g., [Bacha et al., 2023](#); [Tembo et al., 1999](#)). Mafic rocks comprising gabbro and basalt sills, dykes, and flows, of dominantly tholeiitic and alkaline composition, have been mapped in the northwestern arm and Domes region of the Lufilian Arc/Katangan Basin (Figure 1; e.g., [Tembo et al., 1999](#); [Bacha et al., 2023](#); [Kampunzu and Cailteux, 1999](#)), however the volume of magmatism and extent of crustal modification is uncertain.

Overprinting this Neoproterozoic episode of rifting, is the Pan-African Orogeny. Eclogites and whiteschist rocks, interpreted by some as being high-pressure metamorphic assemblages in the Zambezi Belt and Domes regions (Figure 1A), respectively, provide strong evidence for significant crustal thickening (e.g., [Hanson et al., 1994](#); [Unrug, 1983](#); [John and Schenk, 2003](#)). However, whether crustal reworking occurred coherently across the entire region, or localised to certain zones across the Plateau, is uncertain. [Unrug \(1983\)](#) hypothesised that crustal shortening was larger at the western extremity of the Lufilian Arc, where large-scale thrust sheets are present. In the southeast, [Unrug \(1983\)](#) further proposed the existence of a distinct and mechanically-resistant microplate that ultimately gave rise to the arcuate nature of the Lufilian Arc. Others suggest the Zambezi Belt in southeastern Zambia, which contains evidence of eclogites (Figure 1A), experienced the most significant shortening (e.g., [John and Schenk, 2003](#); [Hanson et al., 1994](#)). More recently, through the analysis of mantle seismic anisotropy, [Kounoudis et al. \(2024\)](#) note the lack of a coherent anisotropic fabric across the Lufilian Arc and Zambezi Belt which may be indicative of lateral variations in the extent of shortening/orogenic overprinting at mantle lithospheric depths. Separating the Lufilian and Zambezi Belts, is the Mwembeshi Shear Zone, which is considered by some to be a remnant plate-scale suture

zone between the Congo and Kalahari plates (e.g., *John and Schenk*, 2003; *Coward and Daly*, 1984; *Daly*, 1988). Shear-wave splitting results across the shear-zone in central Zambia, however, lack a discernible fault-parallel anisotropic fabric which is typical of major plate-scale shear/suture zones worldwide (*Kounoudis et al.*, 2024). Key to understanding the region's tectonic evolution, is a detailed picture of crustal structure (i.e., Moho architecture and crustal composition).

In this study, we investigate bulk crustal structure across the Central African Plateau using P-to-S receiver functions recorded on the new Copper Basin Exploration Science (CuBES) seismograph network and surrounding stations. We follow the modified H- $\kappa$  stacking method of *Ogden et al.* (2019) to constrain Moho depth (H) and bulk crustal  $V_P/V_S$  ratio ( $\kappa$ ). Results offer constraints on crustal structure across the region's Archean, Paleoproterozoic and Pan-African orogenic terranes, as well as in areas experiencing Permo-Triassic Karoo rifting and more recent East African Rift-related extension (Figure 1A). Regions of significant crustal re-working may appear to have a deep and highly variable Moho topography. Voluminous frozen magmatic intrusions and the presence of remnant ultramafic oceanic crustal sequences, should manifest as measurable high bulk-crustal  $V_P/V_S$  ratios (e.g., *Ogden et al.*, 2019).

## 2 Tectonic Background

The Central African Plateau, spanning Zambia and the Democratic Republic of Congo, is composed of amalgamated cratonic cores — the Congo, Kalahari and Bangweulu Cratons — separated by a series of Paleozoic-to-Proterozoic-age orogenic belts (Figure 1A). Exposed Archean basement granulite rocks and granitic plutons at the northwestern edge of the Plateau mark the Congo Craton margin, which is flanked by the Pan-African Lufilian Arc (e.g., *Porada*, 1989). To the north of the Plateau, the Bangweulu Block is thought to be a Neoarchean microcontinent composed of Archean and Paleoproterozoic basement re-worked by Phanerozoic tectonic events (e.g., *Begg et al.*, 2009; *De Waele and Mapani*, 2002). The Choma-Kalomo Block, towards the southern edge of the Plateau (Figure 1), is deemed by some workers to be a re-worked portion of the neighbouring Kalahari/Zimbabwe Craton, however, there is thus far no definitive evidence for Archean-age crust in the vicinity (e.g., *Glynn et al.*, 2017). Bordering the cratonic blocks are Paleo- and Meso-Proterozoic orogenic belts (Figure 1A; e.g., *Fritz et al.*, 2013; *Daly*, 1986). These include the Kibaran (1.37–1.30 Ga), Irumide (~1 Ga) and Southern Irumide (~1.2–1.0 Ga) Belts (Figure 1A), which are thought to have experienced varying amounts of crustal shortening during their formation (e.g., *Daly*, 1986; *De Waele and Mapani*, 2002).

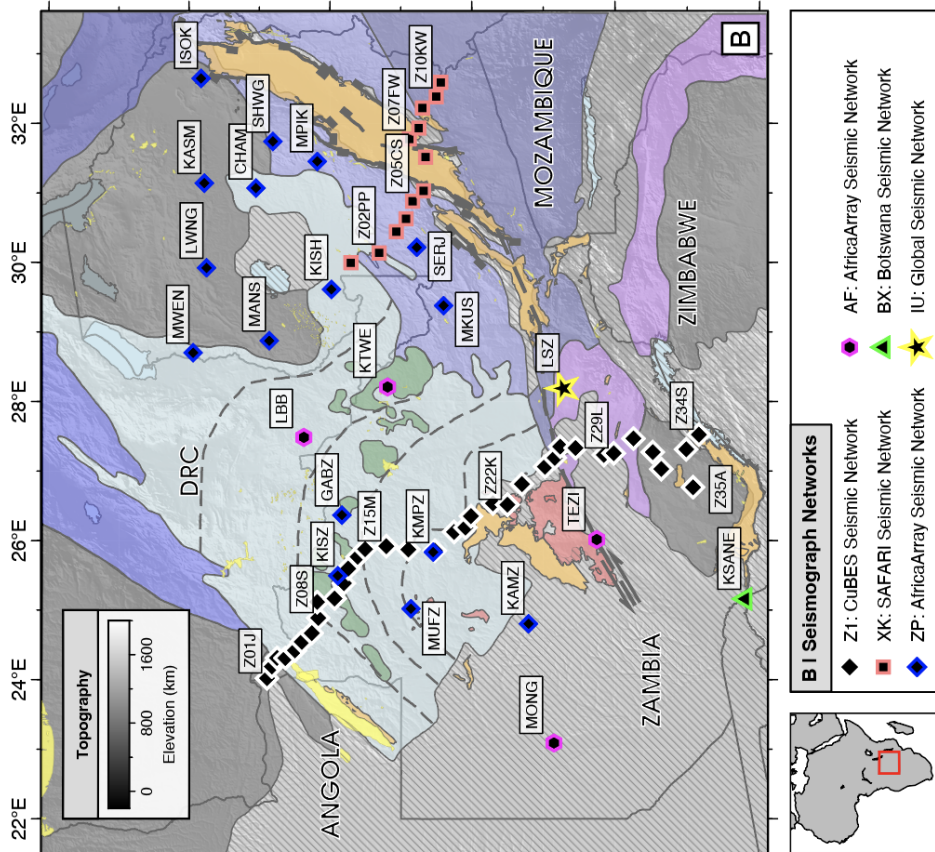
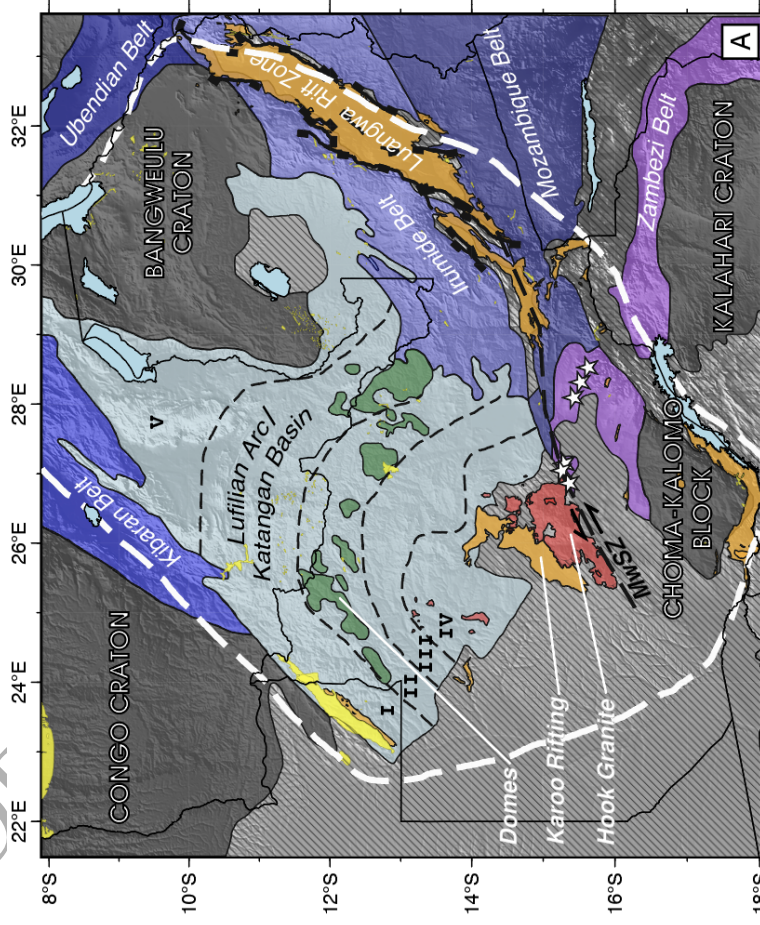


**Figure 1: (A)** Geology and tectonics of the Central African Plateau and surrounding regions. Tectonic units were taken from *Thieme and Johnson* (1981) and *Xu et al.* (2022). Active faults are from *Wedmore et al.* (2022). The white dashed line denotes the outline of the Central African Plateau (*Daly et al.*, 2020). Zones I–V denote the five tectonic subdivisions of the Lufilian Arc/Katangan Basin, as defined by *Porada and Berhorst* (2000): I, External Fold and Thrust Belt; II, Domes Region; III, Synclinorial Belt; IV, Katanga High; V, Katangan Aulacogen. MwSZ: Mwembashi Shear Zone. **(B)** The 2022–2023 CuBEs broadband seismograph network and other surrounding temporary seismograph deployments. The star denotes permanent seismograph station LSZ.

Prior to the Pan-African Orogeny, the Zambezi Belt and Lufilian Arc were characterised by continental rift/ocean basin settings (~880–800 Ma). The Zambezi Belt is thought to mark a suture zone resulting from the closure of either a Neoproterozoic intracratonic basin ([Hanson et al., 1994](#)) or the subduction of a major ocean ~650 Ma ([Hanson et al., 1988; John and Schenk, 2003](#)). The Lufilian Arc marked the location of the broad Neoproterozoic Katangan Basin which evolved into a passive continental margin setting (~800 Ma; e.g., [Porada and Berhorst, 2000](#)). An episode of mafic magmatism at ~750 Ma, affected both terranes, however, estimates of its volume are lacking ([Kampunzu and Cailteux, 1999; Bacha et al., 2023](#)). Subsequently, during the amalgamation of Gondwana (~550 Ma), the Neoproterozoic Zambezi Belt was re-worked, shortened, and overprinted by strongly deformed metasediments and granites ([Begg et al., 2009](#)). Concurrently, the Katangan Basin was re-worked to form the Lufilian Arc (560–550 Ma), which is thought to thrust over the edge of the Congo Craton ([Porada and Berhorst, 2000](#)). The Lufilian Arc/Katangan Basin is divided into 5 tectonic regions (labelled as I to V in Figure 1A): (I) The External Fold and Thrust Belt of dominantly NW-to-NE-vergent thin-skin thrusting; (II) The Domes region is thought to represent the central rift axis during Katangan Basin formation and subsequent locus of greatest compression during the Pan-African Orogeny, in agreement with the presence of Mesoproterozoic basement and high-grade metamorphism (e.g., [Porada and Berhorst, 2000](#)); (III) The Synclinorial Belt and (IV) The Katanga High represent the lower-metamorphic grade regions of the arc. [Porada and Berhorst \(2000\)](#) and [Eglinger et al. \(2016\)](#) postulated the Domes region to be the suture zone between Congo-Kalahari plate convergence, with the Katanga High the northern margin of the overriding Kalahari plate. Zones III and IV are also the proposed location of the microplate hypothesised by [Unrug \(1983\)](#). (V) The Katangan Aulacogen represents the foreland basin. Zones I, II and V are thought to contain mafic igneous intrusions associated with the development of the Katangan Basin in Neoproterozoic times (e.g., [Kampunzu and Cailteux, 1999](#)), however extrusive and intrusive volume estimates are lacking.

The Mwembeshi Shear Zone separates the Lufilian and Zambezi Belts, and was last active in the late Paleozoic (~520 Ma). Whether the shear-zone separates two regions of distinct lithological characteristics is uncertain, however it is assumed to be a plate-scale sinistral feature accommodating the Pan-African convergence of the Kalahari and Congo Cratons (e.g., [de Swardt et al., 1965](#)). North of the shear-zone is the Hook granitic complex, emplaced ~550–530 Ma (e.g., [Naydenov et al., 2014](#)) within the innermost, low metamorphic grade section of the Lufilian Arc (Figure 1A; e.g., [de Swardt et al., 1965](#)). The northern continuation of the Mwembeshi Shear Zone, develops into the Luangwa Rift Valley, formed during Permo-Triassic Karoo rifting (e.g., [Catureanu et al., 2005](#)). Today, the rift is accommodating 0.4–0.6mm/yr of plate motion (e.g., [Wedmore et al., 2022; Daly et al., 2020](#)) associ-

ated with the Cenozoic East African Rift System.

### 3 Previous Geophysical Studies

Across central and southern Africa's cratonic regions (Congo, Kalahari, Tanzania, Kaapvaal and Zimbabwe), previous receiver function and surface-wave studies reveal a generally thick crust (38–43 km) with a pervasive mafic composition for the lower crust ( $V_P/V_S > 1.8$ ; e.g., [Fadel et al., 2018](#); [Julià et al., 2005](#); [Tugume et al., 2013](#); [Kachingwe et al., 2015](#)). A consensus among these previous studies is that there is little evidence for temporal variation in Precambrian crustal structure: Archean and Proterozoic terranes in central and southern Africa have similar thicknesses and crustal compositions. Across the Central African Plateau specifically, P-to-S receiver functions ([Sun et al., 2021](#)) and their joint inversion with surface waves ([Kachingwe et al., 2015](#)), conducted on previous seismograph deployments in the region (Figure 1B), reveal an approximate  $\pm 10$  km variation in Moho depth: ~35 km in southern Zambia (e.g., Zambezi Belt), to 48 km across northern Zambia (e.g., Irumide Belt and Lufilian Arc). [Kachingwe et al. \(2015\)](#) and [Sun et al. \(2021\)](#) also find Poisson's ratios between 0.20–0.25 ( $\kappa = 1.633\text{--}1.732$ ) for the majority of stations across the Plateau, indicative of a dominantly felsic bulk-crustal composition. More recently, using CuBES project data [Kounoudis et al. \(2024\)](#) conducted a shear-wave splitting analysis, illuminating lithospheric anisotropic fabrics across the Plateau. Below the Pan-African Lufilian Arc, [Kounoudis et al. \(2024\)](#) observe abrupt changes in splitting parameters (delay times and fast directions) that are attributed to either multiple episodes of deformation during the Pan-African Orogeny, or the variable overprinting of pre-existing extensional fabrics across the region. The greatest variability in anisotropy lies near the Domes region ([Kounoudis et al., 2024](#)).

Across the Mwembeshi Shear Zone in central Zambia, there is a lack of deep-penetrating geophysical constraints, with the exception of two H- $\kappa$  stacking measurements at stations TEZI and LSZ, which lie within 20 km and 100 km of the shear-zone, respectively; [Kachingwe et al. \(2015\)](#) image a uniform Moho depth of ~39 km at both stations. Using shear-wave splitting, [Kounoudis et al. \(2024\)](#) find a lack of fault-parallel anisotropy across the Mwembeshi Shear Zone. The authors attribute this observation to the fault either being a too narrow, thin-skinned, crustal-scale feature, and/or lacking in sufficient fault parallel shear-strain to form a lithospheric deformation fabric discernible using shear-wave splitting. Along the northward continuation of the shear-zone, towards the Luangwa Rift valley, magnetotelluric imaging ([Sarafian et al., 2018](#)) reveals a conductive lithospheric discontinuity interpreted as the Mwembeshi Shear Zone. However, there is no discernible Moho depth contrast across the rift

valley/shear-zone observed in P-to-S receiver functions using data from the SAFARI seismic network (Figure 1B; [Sun et al., 2021](#)).  $V_P/V_S$  in this region is also akin to globally averaged continental crust (~1.76; [Sun et al., 2021](#)), with rifting thus unlikely to have been accompanied by significant mafic lower crustal intrusions. This is corroborated by the ambient noise crustal tomography study of [Wang et al. \(2019\)](#), who find at most 2 km of crustal thinning below the rift valley, and wavespeeds akin to other non-volcanic regions. Nevertheless, slow-wavespeeds at mid-crustal depths below the Luangwa Rift zone do exist in some isolated localites, and may be attributed to elevated temperatures, fluid-filled deep faults, and/or magmatic intrusions ([Wang et al., 2019](#)).

## 4 Data and Methods

### 4.1 Seismograph Networks

Prior to the CuBES seismograph network, station coverage across western and southern Zambia was limited to a few sparsely distributed temporary stations. The CuBES network addresses this data gap and consists of 35 broadband seismograph stations deployed for 18 months from May 2022 to November 2023 along a ~800 km profile from the edge of the Congo Craton in northwestern Zambia, to the shore of Lake Kariba in southern Zambia (Figure 1). The network consists of 12 CMG-6TD, 21 CMG-ESP and two CMG-3T Guralp sensors, with flat responses to periods of 30 s, 60 s and 120 s, respectively. During the deployment, data recovery was ~96%. Sensor malfunction at station Z26M resulted in no recorded data at this locality. CuBES stations are supplemented with data from stations across Zambia and the surrounding area, including AF ([Penn State University, 2004](#)), IU ([Albuquerque Seismological Laboratory/USGS, 2014](#)), BX/NR ([Botswana Geoscience Institute, 2001](#)), XK ([Gao et al., 2012](#)) and ZP ([Nyblade, 2007](#)) seismic networks, allowing 70 stations to be analysed.

### 4.2 Teleseismic dataset

Following the processing method of [Ogden et al. \(2019\)](#), seismograms for earthquakes of  $M_W \geq 4.5$  within 30–90° epicentral distance were selected for P receiver function analysis. Additionally, seismograms for earthquakes of  $M_W \geq 5.5$  at epicentral distances >60° were selected for PP receiver functions. Seismograms were filtered using a 0.04 Hz to 3 Hz Butterworth bandpass filter. If the P-wave signal-to-noise ratio was >2, earthquake-station pairs were provisionally accepted and then visually

inspected to remove erroneous traces, allowing 2069 acceptable-quality three component seismograms. Receiver functions were calculated using the time-domain iterative deconvolution method of [Ligorria and Ammon \(1999\)](#), where a spike train is iteratively updated using a least-squares minimisation until either a maximum number of spikes is reached (200) or the iteration improvement is less than a threshold (0.001%) from the previous iteration. The Gaussian width factor controls the frequency content of the receiver function via a low-pass Gaussian filter applied in the frequency domain using a fast Fourier transform; a larger value indicates a larger bandwidth. The frequency (in Hz) of the estimated receiver function is approximately half that of the Gaussian width. To identify unstable receiver functions, we calculate the variance of the misfit between the receiver function estimate convolved with the observed vertical component seismogram, and the observed radial seismogram, divided by the variance of the observed radial seismogram, and converted to variance reduction expressed as a percentage (where 100% represents a receiver function that perfectly reproduces the observed radial seismogram). For each earthquake-station pair we generate a suite of 17 receiver functions with Gaussian widths of 0.8 to 4.0 at intervals of 0.2. Receiver functions with a final variance reduction of  $\leq 80\%$  were rejected automatically along with all other frequencies for that earthquake-station pair. Receiver functions were visually inspected to remove remaining poor quality traces such as those with unrealistically large amplitude peaks at later time periods, or waveforms with cyclical reverberations (likely generated by near-surface velocity contrasts). Additionally, the k-Shape algorithm ([Paparrizos and Gravano, 2015](#); [Tavenard et al., 2020](#)), which is based on normalised cross-correlations for shape-based clustering of time series, was used to independently identify and remove any remaining receiver functions with similar undesirable waveform characteristics. Stations with  $< 6$  remaining events were discarded, leaving 1325 earthquake-station pairs from 65 stations for  $H-\kappa$  stacking analysis.

### 4.3 Receiver functions and $H-\kappa$ stacking

Receiver functions contain P-to-S wave conversions produced at velocity discontinuities beneath seismograph stations, recorded in the P-wave coda of teleseismic earthquakes (e.g., [Phinney, 1964](#); [Langston, 1977](#)). Of particular interest are the primary Moho P-to-S conversion ( $Ps$ ) and subsequent crustal reverberations ( $PpPs$ ,  $PpSs + PsPs$ ). Crustal thickness ( $H$ ) and bulk crustal  $V_P/V_S$  ratios ( $\kappa$ ; averaged over the slowness and back-azimuths sampled by the source-station ray-paths) can be estimated using the arrival times of these three phases via the  $H-\kappa$  stacking procedure of [Zhu and Kanamori \(2000\)](#). The method involves stacking amplitudes along predicted moveout curves for the Moho conversion and subsequent reverberations. A grid-search is performed over a range of geolog-

ically plausible values of  $H$  and  $\kappa$  to produce the stacking surface  $s(H, \kappa)$ :

$$s(H, \kappa) = \sum_{j=1}^N w_1 r_j(t_1) + w_2 r_j(t_2) - w_3 r_j(t_3), \quad (1)$$

where  $N$  is the number of receiver functions;  $w_1, w_2, w_3$  are stacking weights (where  $\sum w = 1$ ),  $r_j(t_i)$  are the amplitudes at the arrival times for each of the arrivals evaluated.  $t_1, t_2$ , and  $t_3$  are the travel times of the  $Ps$ ,  $PpPs$ , and  $PsPs + PpSs$  phases, respectively:

$$t_1 = H \left[ \sqrt{\frac{1}{V_S^2} - p^2} - \sqrt{\frac{1}{V_P^2} - p^2} \right], \quad (2)$$

$$t_2 = H \left[ \sqrt{\frac{1}{V_S^2} - p^2} + \sqrt{\frac{1}{V_P^2} - p^2} \right], \quad (3)$$

$$t_3 = 2H \sqrt{\frac{1}{V_S^2} - p^2}, \quad (4)$$

where  $p$  is the ray parameter and  $V_P$  and  $V_S$  are bulk crustal P- and S-wave velocities, respectively. The optimal combination of  $H$  and  $\kappa$  is taken to be where  $s(H, \kappa)$  is maximised. [Ogden et al. \(2019\)](#) demonstrated that  $H$ - $\kappa$  stacking is sensitive to user-provided input parameters such as  $V_P$  (6.2–6.8 km/s), the weighting ( $w_i$ ) of each phase, the choice of stacking strategy (linear versus phase-weighted ([Schimmel and Paulsen, 1997](#))), receiver function frequency content, and the sample of receiver functions which are stacked. We therefore follow the modified  $H$ - $\kappa$  stacking method of [Ogden et al. \(2019\)](#) which repeats the standard  $H$ - $\kappa$  stacking procedure 1000 times, altering the input parameters within geologically plausible limits and resampling the receiver function subset with each repeat using hierarchical cluster analysis to obtain an estimate of  $H$  and  $\kappa$  (e.g. station Z08S; Figure 2). Individual measurement errors in  $H$  and  $\kappa$  are calculated from the 95% contour of the  $s(H, \kappa)$  surface. However, the standard deviation of  $H$  and  $\kappa$  calculated from the  $\leq 1000$   $H$ - $\kappa$  measurements generally represent more realistic error estimates. We therefore refer to the mean values of  $H$  and  $\kappa$ , and associated standard deviations, as the final results and errors for a station, rather than the individual measurement selected by cluster analysis. Ten quality control criteria are used to assess the reliability of  $H$ - $\kappa$  stacking at a station (see [Ogden and Bastow, 2022](#), for a complete list of these criteria). The pass or fail outcomes of each criteria are illustrated by green or red circles in panels a–i of all subsequent station result plots (e.g., Figure 2). For the 19 stations where  $\kappa < 1.7$ , with the original  $\kappa$  grid-search range (1.65–2.2),

a lower  $\kappa$  grid-search range of 1.55–2.1 is used to ensure that the full  $H-\kappa$  space is explored and that error surfaces are closed.

For each repeat, one receiver function frequency is selected randomly, from the 0.4–2 Hz range. A station with a stable solution at 2 Hz is also inherently stable at 0.4 Hz. However, if a station result is unstable after 1000 repeats using  $\leq 2$  Hz data, reducing the frequency of the receiver functions can lead to improved results (*Ogden et al., 2019*); repeats using higher frequencies can be systematically discarded until a stable result is achieved at a maximum receiver function frequency ( $F_{max}$ ). Achieving a stable result at all frequencies up to and including 2 Hz suggests that the Moho discontinuity is likely sharp; stations that work at reduced frequencies ( $\leq F_{max}$ ) either have a more gradational Moho discontinuity, or complex intra-crustal structure (e.g., *Ogden et al., 2019, 2021, 2023*).  $F_{max}$  is therefore an indicator of Moho sharpness. Stations where reliable  $H-\kappa$  stacking estimates are achieved using reduced frequency receiver functions inherently have larger individual measurement errors in  $H$  and  $\kappa$ , and have reduced vertical resolution due to sampling lower frequency receiver functions. For example, the cluster analysis derived estimate of crustal thickness for station Z08S at  $F_{max} = 2.0\text{ Hz}$  is  $40.5 \pm 0.4\text{ km}$  (Figure 2a), compared to  $41.9 \pm 2.2\text{ km}$  when  $F_{max} = 0.4\text{ Hz}$ . However, the equivalent mean crustal thickness estimates for  $F_{max} = 2.0\text{ Hz}$  and  $F_{max} = 0.4\text{ Hz}$ , are  $40.8 \pm 1.5\text{ km}$  (Figure 2) and  $41.2 \pm 1.5\text{ km}$ , which are comparatively similar and further demonstrate why using mean values of  $H$  and  $\kappa$  are more suitable (*Ogden and Bastow, 2022*).

Following *Ogden et al. (2023)*, we pay particular attention to three receiver function quality indicators: amplitude comparison estimate (ACE), cross-correlation coefficient (CCC) and iterative deconvolution variance reduction (IDVAR). ACE is a measure of the impulsivity of the  $P_s$  arrival, and is calculated by comparing the amplitude at the predicted  $t_1$  arrival time (theoretically the picked  $P_s$  arrival), with the root-mean-square (RMS) amplitude of the background signal in the receiver function between  $t_1 + 2\text{ s}$  and  $t_2 - 2\text{ s}$ . CCC tests for the effect of noise and backazimuthal variation at each station by measuring the mean cross-correlation coefficient on all possible pairs of receiver functions with the same frequency; this is repeated for each different frequency of receiver function. IDVAR is the mean value of the iterative deconvolution variance reduction for all receiver functions calculated at  $F_{max}$ . Larger values of these analytics indicate a larger amplitude  $P_s$  conversion and/or receiver functions which are relatively simple with homogeneous crustal structure beneath a station. Conversely, decreased analytic values might indicate the presence of a more gradational Moho or back-azimuthally variable crustal structure beneath the station.

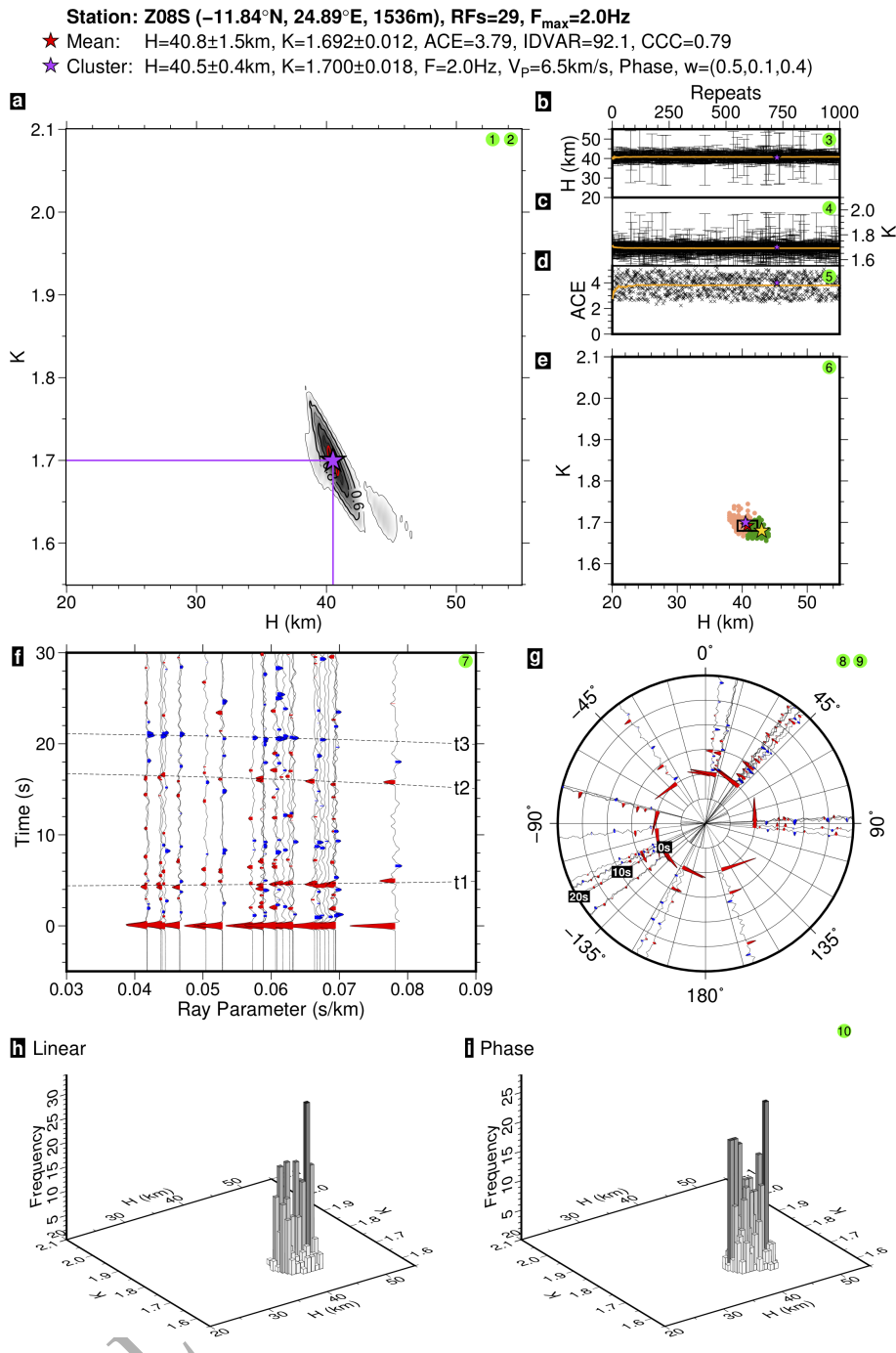


**Figure 2:** Successful  $H-\kappa$  result for station Z08S in the western arm of the Lufilian Arc/Katangan Basin (Figure 1) for receiver function frequencies of  $\leq 2\text{ Hz}$ . Numbered (1–10) dots refer to pass (green) or fail (red) status of the ten criteria. (a) The  $s(H, \kappa)$  stacking surface associated with the result selected using hierarchical cluster analysis. Crustal thickness (b),  $V_P/V_S$  ratio (c), and ACE (d) for each of the 1000  $H-\kappa$  solutions. (e) All 1000  $H-\kappa$  solutions with colour representing the cluster that a result is assigned to. The purple star is the combination of  $H$  and  $\kappa$  selected by the cluster analysis and plotted in (a), the red star (beneath the purple star) is the mean of  $H$  and  $\kappa$  from the 1000 repeats, the yellow star is the mode combination of  $H$  and  $\kappa$ , the black box marks one standard deviation in  $H$  and  $\kappa$ . Accepted receiver functions plotted by horizontal slowness (f), and backazimuth (g),  $t_1$ ,  $t_2$  and  $t_3$  denote the predicted arrival times using the mean  $H$  and  $\kappa$  estimates. The peaks/troughs are coloured when their amplitude is  $>20\%$  of the P arrival amplitude. Distribution of (h) linear and (i) phase weighted stacking results.

## 5 Results

Of the 70 stations analysed in this study, 56 produced a reliable  $H-\kappa$  stacking result (Figure 3A; Table 1). For the CuBES network, 26 of 35 seismograph stations produced a reliable result using the full frequency range of receiver functions, indicating strong evidence of a sharp Moho beneath these stations. Four stations along the profile did not yield reliable results at any frequency: failure at station Z28C is likely due to the presence of substantial Quaternary alluvium, whereas, failure at stations Z14M, Z31K and Z33S (red symbols in Figure 3A) is likely attributed to more complex crustal structure which will be discussed later. Receiver function analytics are generally high across the network, implying relatively high amplitude  $P_s$  conversions associated with a sharp Moho and relatively simple crustal structure (ACE), and high receiver function similarity (CCC) as a function of earthquake backazimuth and epicentral distance (Figure 4). IDVAR is  $\geq 90$  for all stations indicating high quality receiver functions and that all stations passed the IDVAR criteria.  $H-\kappa$  results for all successful stations are presented in the supplementary materials (Figures S1–S55).

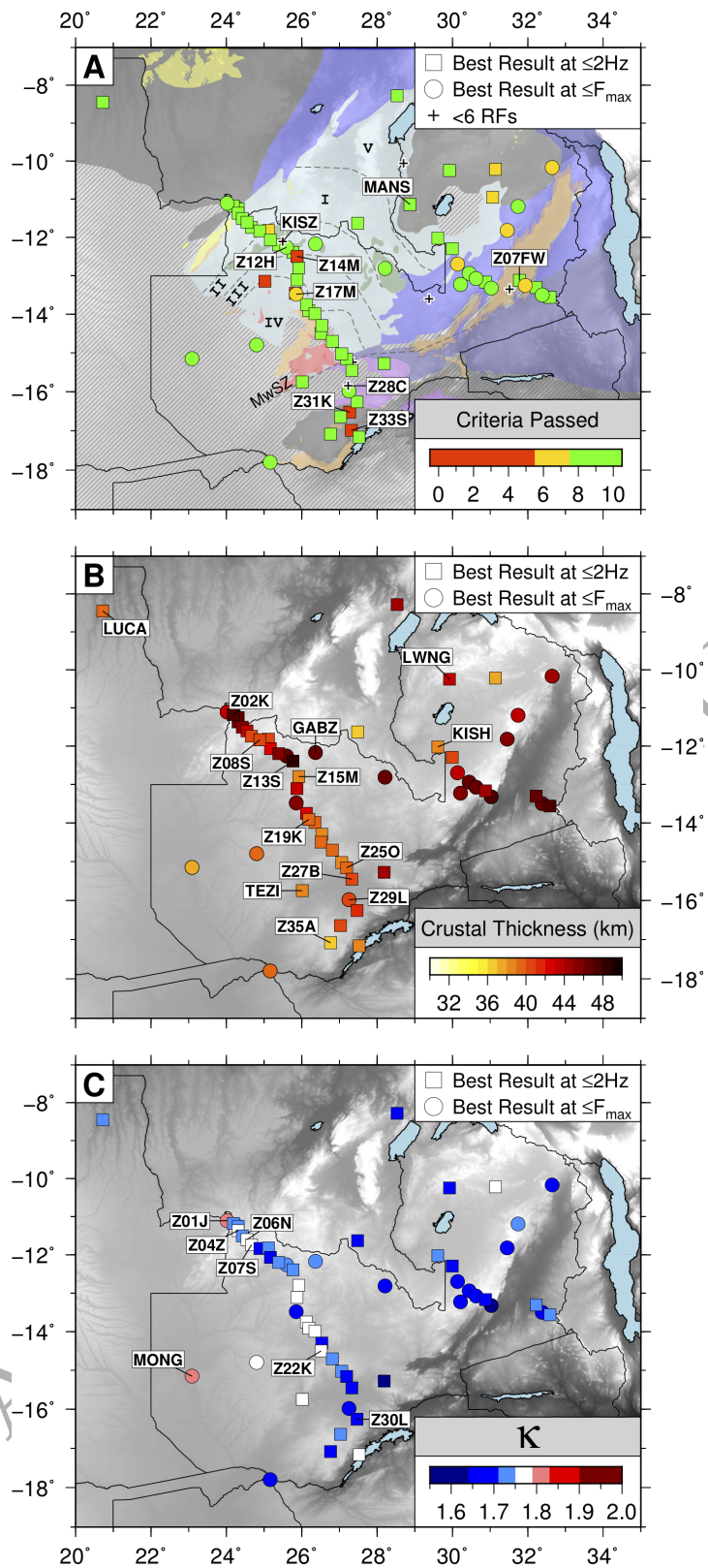


**Figure 3:** (a) Criteria passed for each station with six or more acceptable receiver functions. Colours indicate geological units as described in Figure 1. Zones I-V described in Section 2. MwSZ: Mwem-beshi Shear Zone. (b) Crustal thickness below the study area. (c)  $V_P/V_S$  ratio below each station where a result was reliable.

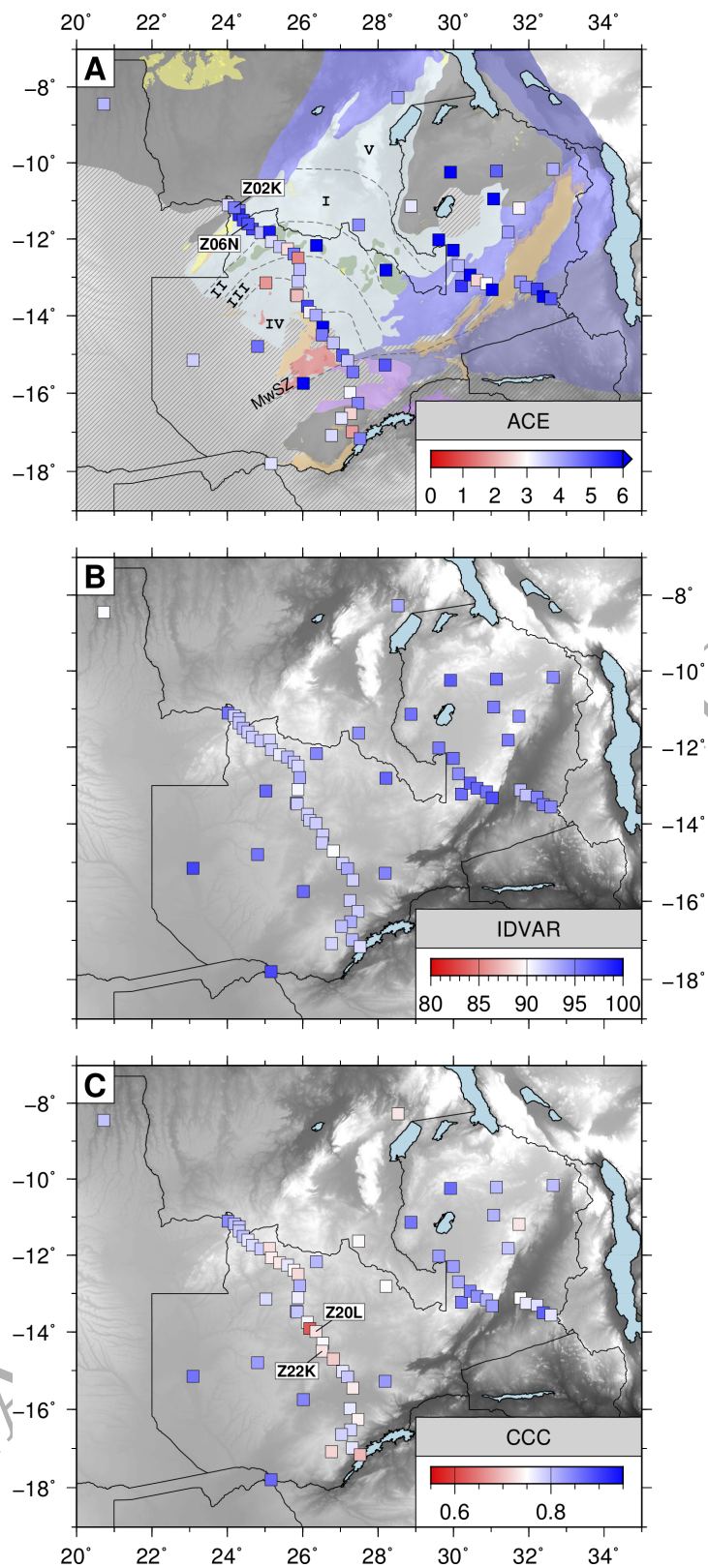


**Figure 4:** (a) ACE, (b) IDVAR and (c) CCC for each station analysed in this study with six or more acceptable receiver functions, including stations for which a reliable  $H-\kappa$  result could not be achieved. Station quality indicator values are obtained from either their result achieved using  $\leq 2$  Hz receiver functions, or using  $\leq F_{max}$  data if this produced a stable result. In (a), colours indicate geological units as described in Figure 1. Zones I-V described in Section 2. MwSZ: Mwembeshi Shear Zone.

**Table 1:** Complete H- $\kappa$  results for all successful stations. RF: number of receiver functions, CP: criteria passed.

Station	Lat (°)	Long (°)	RF	CP	H (km)	$\kappa$	ACE	CCC	IDVAR
Z01J	-11.11	24.02	11	8	43.9±6.7	1.815±0.117	3.47	0.84	95.5
Z02K	-11.18	24.19	31	10	47.8±2.3	1.734±0.034	4.54	0.80	92.0
Z03H	-11.25	24.31	38	9	46.7±2.8	1.746±0.048	4.52	0.80	92.3
Z04Z	-11.37	24.31	21	10	46.9±2.4	1.752±0.035	5.60	0.79	92.1
Z05C	-11.51	24.42	17	10	45.5±2.1	1.741±0.023	5.23	0.80	92.8
Z06N	-11.60	24.55	31	10	43.3±1.7	1.762±0.015	5.01	0.77	91.9
Z07S	-11.74	24.67	10	8	40.5±3.1	1.780±0.068	5.23	0.78	92.0
Z08S	-11.84	24.89	29	10	40.8±1.5	1.692±0.012	3.79	0.79	92.1
Z09L	-11.82	25.12	7	7	40.0±3.2	1.727±0.072	5.81	0.73	91.7
Z10C	-12.07	25.17	27	10	42.9±1.6	1.702±0.016	3.40	0.74	91.9
Z11N	-12.20	25.39	24	8	45.4±3.3	1.739±0.064	3.62	0.73	90.8
Z12H	-12.26	25.60	29	8	46.2±2.9	1.745±0.045	2.60	0.77	92.7
Z13S	-12.39	25.77	31	8	48.1±3.5	1.729±0.057	4.57	0.74	92.3
Z15M	-12.80	25.92	9	10	38.5±2.3	1.763±0.042	3.76	0.81	93.4
Z16N	-13.11	25.87	20	8	43.3±3.6	1.779±0.087	3.64	0.76	90.4
Z17M	-13.48	25.85	27	7	45.7±5.0	1.659±0.045	2.23	0.79	91.9
Z18K	-13.75	26.12	24	10	42.3±1.9	1.767±0.023	5.18	0.76	91.8
Z19K	-13.91	26.19	9	9	39.6±2.3	1.762±0.053	3.18	0.62	91.9
Z20L	-13.99	26.35	32	10	39.1±1.5	1.776±0.022	3.95	0.73	92.0
Z21G	-14.30	26.53	25	10	38.5±1.5	1.702±0.012	6.51	0.76	91.9
Z22K	-14.50	26.52	31	10	39.0±1.5	1.760±0.015	4.55	0.73	92.0
Z23K	-14.70	26.81	26	10	39.4±1.5	1.748±0.028	3.71	0.71	90.1
Z24M	-15.02	27.06	26	10	38.6±2.3	1.729±0.038	5.00	0.77	91.8
Z25O	-15.16	27.19	26	9	39.5±1.8	1.680±0.029	3.66	0.79	93.3
Z27B	-15.45	27.33	27	10	40.2±1.5	1.651±0.023	4.63	0.73	91.8
Z29L	-15.98	27.26	18	10	40.2±2.1	1.707±0.037	3.12	0.77	91.9
Z30L	-16.26	27.47	34	9	41.9±2.6	1.647±0.042	4.45	0.74	91.9
Z32B	-16.64	27.03	25	8	40.0±3.5	1.745±0.077	3.29	0.79	92.4
Z34S	-17.16	27.52	9	8	38.2±3.6	1.750±0.094	4.48	0.69	91.4

Table 1 continued

Station	Lat (°)	Long (°)	RF	CP	H (km)	$\kappa$	ACE	CCC	IDVAR
Z35A	-17.08	26.77	10	8	36.6±4.1	1.666±0.097	3.44	0.72	91.7
GABZ	-12.17	26.37	14	10	46.1±1.9	1.735±0.016	9.43	0.81	94.8
ISOK	-10.17	32.65	13	7	44.1±4.9	1.643±0.074	3.95	0.80	94.5
KAMZ	-14.79	24.80	6	10	39.4±1.9	1.785±0.046	4.67	0.83	95.4
KASM	-10.22	31.14	13	6	37.6±6.4	1.768±0.169	4.89	0.80	95.9
KISH	-12.02	29.61	18	10	38.1±1.4	1.714±0.015	6.54	0.83	95.2
KTWE	-12.81	28.21	13	10	46.1±2.1	1.643±0.025	6.06	0.75	96.0
LBB	-11.63	27.49	14	9	36.7±1.8	1.686±0.027	4.37	0.74	94.3
LSZ	-15.28	28.19	84	10	44.7±1.7	1.606±0.028	5.01	0.83	94.8
LUCA	-8.45	20.72	17	10	39.5±1.6	1.719±0.026	3.84	0.80	90.1
LWNG	-10.25	29.92	10	10	43.2±1.6	1.708±0.013	6.30	0.87	96.4
MONG	-15.15	23.09	11	8	37.6±2.0	1.812±0.036	3.56	0.86	97.4
MPIK	-11.82	31.45	10	7	45.3±4.3	1.707±0.070	4.15	0.80	95.2
NE206	-17.80	25.16	16	9	39.0±1.8	1.665±0.032	3.37	0.87	97.2
PWET	-8.28	28.53	10	8	44.5±4.1	1.683±0.058	4.10	0.73	93.4
SERJ	-13.23	30.22	13	10	45.8±2.3	1.682±0.026	5.44	0.85	95.7
SHWG	-11.19	31.74	13	9	43.5±2.0	1.740±0.038	2.89	0.73	94.5
TEZI	-15.75	26.02	42	10	38.1±1.5	1.755±0.012	8.00	0.84	95.9
Z01TG	-12.30	29.99	24	8	40.0±3.3	1.695±0.075	6.94	0.83	95.6
Z02PP	-12.70	30.14	25	7	43.5±3.3	1.706±0.074	3.83	0.82	94.5
Z03CK	-12.94	30.44	18	8	46.3±4.2	1.698±0.086	6.04	0.85	96.1
Z04NN	-13.07	30.63	22	9	46.5±2.4	1.672±0.034	2.50	0.84	96.0
Z05CS	-13.17	30.88	17	8	44.6±3.5	1.696±0.055	3.03	0.81	95.5
Z06LW	-13.32	31.03	7	10	47.3±2.3	1.629±0.026	6.50	0.82	96.9
Z09CG	-13.31	32.22	18	10	46.8±1.8	1.712±0.015	5.28	0.78	94.9
Z10KW	-13.50	32.38	10	10	46.9±2.3	1.706±0.040	6.85	0.87	95.2
Z11CP	-13.56	32.59	15	10	47.7±1.8	1.723±0.014	5.03	0.77	94.6

## 5.1 Crustal Thickness

Crustal thickness is 45–49 km in northwestern Zambia (Figure 3B) on, or approaching, the edge of the Congo Craton (e.g.,  $H_{Z02K} = 47.8 \pm 2.3$  km), gradually thinning ( $H_{Z08S} = 40.8 \pm 1.5$  km) to the south, towards the center of the Lufilian Arc/Katangan Basin (Figure 5). In contrast, station LUCA in Angola (Figure 3A), which is located in the centre of the Congo Craton, has a Moho depth of  $39.5 \pm 1.6$  km (Figure S38), corroborating the H- $\kappa$  stacking study of *Kachingwe et al.* (2015) who find a Moho depth of  $38.6 \pm 1.9$  km. Impulsive primary Moho  $P_s$  conversions with high ACE values (>4; Figure 4A) are observed at stations in northwestern Zambia (e.g., Z02K and Z06N; Figures S2f and S6f), indicating the presence of a relatively sharp Moho.

Near the Domes region of the Lufilian Arc/Katangan Basin (Figure 1A), H- $\kappa$  stacking becomes less reliable, and works best at reduced frequencies for some stations (e.g., Z12H, Z17M). Additionally, no stable result is achieved at station Z14M due to inconsistent  $P_s$  Moho conversions and unclear Moho reverberations. Receiver functions at station Z17M are dominated by several positive amplitude arrivals between 2–8 s (Figure S15f), resulting in a low ACE value (2.23; Figure 4A). Weak Moho reverberations were also found at nearby station KISZ by *Kachingwe et al.* (2015); we were unable to produce a reliable result for this station in our analysis due to an insufficient number of receiver functions. Crustal thickness is highly variable near the Domes region (Figure 5): at station Z15M the Moho depth is  $38.5 \pm 2.3$  km compared to  $48.1 \pm 3.5$  km at station Z13S, located ~50 km away (Figure 1B). Station GABZ, has a crustal thickness of  $46.1 \pm 1.9$  km, in agreement with that of Z13S.

Along the central section of the CuBES profile (central Zambia), between stations Z19K and Z27B, high quality H- $\kappa$  stacking results (Figure 3A) reveal a consistent Moho topography and a crustal thickness that is <10 km thinner (38.5–40.2 km) in comparison to the northern section of the line. Africa Array station TEZI, ~150 km west of the CuBES profile, displays some of the clearest P-to-S Moho conversions observed in Zambia (Figure S46f). Consequently, the station has a very reliable crustal thickness estimate of  $38.1 \pm 1.5$  km and very high ACE (8.00) and CCC (0.84) values. TEZI is situated close to the Mwembeshi Shear Zone and the Moho depth is consistent with that obtained at the along-strike station Z25O ( $39.4 \pm 1.7$  km). Although there is no discernible change in crustal thickness across the Mwembeshi Shear Zone, H- $\kappa$  stacking estimates are generally less reliable south compared to north of the shear-zone (some stations do not pass the >5 criteria threshold; i.e., stations Z31K and Z33S). Where a result is estimated at station Z29L, crustal thickness is  $40.2 \pm 2.1$  km. The southernmost extremity of the profile (Z35A) on the Choma-Kaloma granitic block has the thinnest crust observed on the CuBES profile ( $36.6 \pm 4.1$  km).

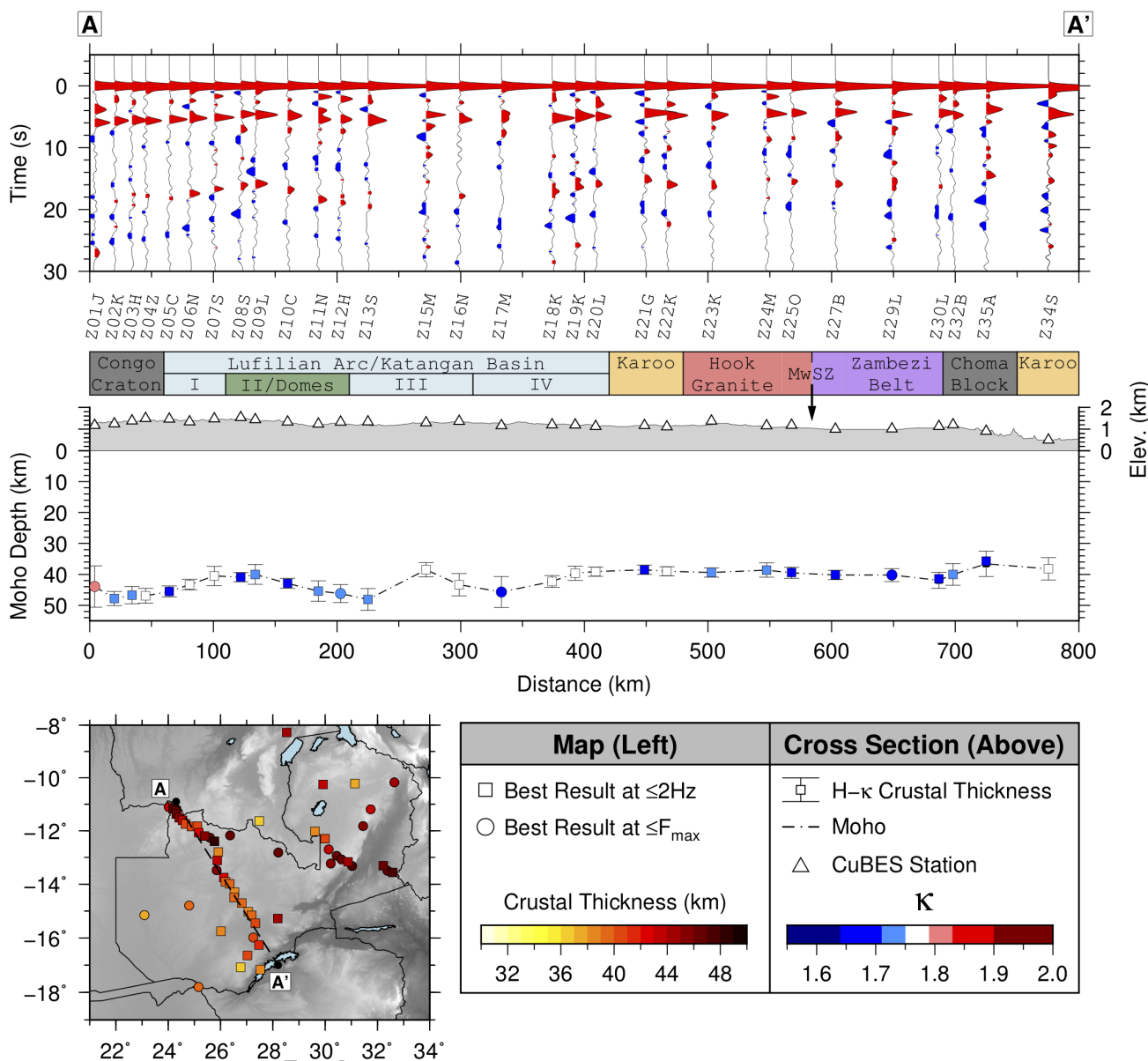


**Figure 5:** Top: Stacked receiver functions for stations along profile A–A'. Centre: Crustal thickness cross-section across the Central African Plateau in central Zambia. Each station result is coloured by its corresponding  $V_P/V_S$  ratio. Tectonic zones according to Figure 1 are plotted above the elevation profile. The profile orientation (A–A') is shown on the bottom left map along with crustal thickness measurements. MwSZ: Mwembeshi Shear Zone, I–IV: Zones of the Lufilian Arc/Katangan Basin.

In eastern Zambia, estimates from stations of the SAFARI network suggest a crustal thickness of ~45 km to the east, and ~48 km to the west of the Luangwa Rift Zone. Clear  $P_s$  conversions and high ACE values for these stations indicate a sharp Moho is present either side of the rift. In this study, we cannot obtain a reliable  $H-\kappa$  measurement from directly beneath the Luangwa Rift Zone. Receiver functions at station Z07FW display multiple peaks (e.g., ~2 s, ~4 s, ~10 s, ~12 s and ~16 s; Figure S56a) which may be masking Moho-generated reverberations thus affecting our  $H-\kappa$  estimate and reducing the CCC value for the station (Figure 4c). However, the  $H-\kappa$  stacking study of [Sun et al. \(2021\)](#) and surface wave study of [Wang et al. \(2019\)](#) both noted no discernible thinning below Luangwa compared to surrounding regions ( $H_{Z07FW} \sim 40$  km). North of the Luangwa Rift, stations on the Bangwelu craton have crustal thickness estimates ranging from  $38.1 \pm 1.4$  km (KISH) to  $43.2 \pm 1.6$  km (LWNG), slightly thinner than the 43.9 km average estimate of [Kachingwe et al. \(2015\)](#) for the Bangwelu craton. Both of these stations have high ACE, CCC and IDVAR values (Figure 4), consistent with a sharp Moho and relatively simple crustal structure.

## 5.2 Crustal Composition

Across the majority of the CuBES seismograph network,  $V_P/V_S$  ratios ( $\kappa$ ) are relatively consistent and generally below the global continental average (1.765), ranging from 1.647 (Z30L) to 1.815 (Z01J; Figure 3C).  $V_P/V_S$  is felsic ( $\kappa \leq 1.75$ ) for 20 CuBES stations, and intermediate (1.75–1.79) for a further 9 stations located in the northernmost (Z04Z–Z07S) and central (Z15M–Z22K) sections of the CuBES profile. Only one CuBES station, Z01J at the Congo Craton margin, has a  $\kappa$  estimate which is mafic ( $1.815 \pm 0.117$ ). Elsewhere, elevated  $V_P/V_S$  ( $> 1.8$ ) is found only at station MONG in the southeastern part of the Lufilian Arc/Katangan Basin. Our results generally agree with the  $H-\kappa$  study of [Kachingwe et al. \(2015\)](#) who find Poisson's ratio's between 0.20–0.25 ( $\kappa = 1.633 - 1.732$ ) for the majority of stations across the Central African Plateau. However, nowhere below the region, do previous studies (e.g., [Kachingwe et al., 2015](#); [Sun et al., 2021](#)) measure  $V_P/V_S > 1.8$  (equivalent to a Poisson's ratio above ~0.28). The largely low  $V_P/V_S$  ratios ( $< 1.765$ ) are consistent with those observed globally in regions composed of Quartz-rich granitic basement geology (e.g., [Thompson et al., 2010](#); [Lowry and Pérez-Gussinyé, 2011](#); [Ogden et al., 2019](#)) and experimentally derived estimates of granites (e.g., [Christensen, 1996](#)). In the Irumide Belt flanking the Permo-Triassic Luangwa Rift Zone, our low  $V_P/V_S$  results (Figure 3C) corroborate the receiver function study of [Sun et al. \(2021\)](#).

## 6 Discussion

### 6.1 Implications for the Development of the Katangan and Zambezi Basins

The Katangan Basin is thought to have formed as a result of rifting during the Neoproterozoic (e.g., *Unrug*, 1983; *Porada*, 1989), and may have involved the concurrent development of a large igneous province (LIP) (e.g., *Kampunzu and Cailteux*, 1999; *Bacha et al.*, 2023; *Tembo et al.*, 1999). Evidence of Neoproterozoic rift, and possibly plume-related, pillow lavas, dikes and sills, dated at ~765–735 Ma have been observed across a 450x600 km-wide region in northwest Zambia and the southeastern Democratic Republic of Congo (Zones I and II; Figure 1; e.g., *Cosi et al.*, 1992; *Bacha et al.*, 2023). However, the volume and extent of crustal magmatic modification is uncertain, including whether continental rifting evolved into the proto-oceanic stage (e.g., *Porada and Berhorst*, 2000; *Kampunzu and Cailteux*, 1999). Similarly, the contemporaneous development of the Zambezi Basin in southeastern Zambia is also thought to have been accompanied by mafic magmatism at ~860 Ma and ~750 Ma (e.g., *Holwell et al.*, 2017), however, it is postulated to have involved the formation of a major ocean that was later subducted (e.g., *John and Schenk*, 2003). Bulk-crustal  $V_P/V_S$  ratios >1.8 are often measured in regions that have experienced voluminous mafic magmatism (e.g., *Lowry and Pérez-Gussinyé*, 2011), such as below the Cenozoic flood basalt-capped Ethiopian Plateau (e.g., *Ogden et al.*, 2019; *Stuart et al.*, 2006), Deccan Trapps (e.g., *Reddy and Rao*, 2013), Emeishan LIP (*Chen et al.*, 2015), and below magmatic rifts (e.g., *Daly et al.*, 2008). Oceanic crust is also characterised by similarly elevated  $V_P/V_S$  ratios (>1.85; e.g., *Lowry and Pérez-Gussinyé*, 2011; *Christensen*, 1996).

Consistently low bulk-crustal  $V_P/V_S$  ratios (~1.61–1.765) are observed in Figures 3C and 5 across the Katangan Basin. Our results are therefore indicative of continental crust largely unmodified by voluminous mafic magmatism, arguing against a significant addition of gabbroic material to the crust — a process typical in voluminous LIP development (e.g., *Mackenzie et al.*, 2006). As well as bulk crustal  $V_P/V_S$  ratios, receiver function frequencies offer an additional proxy for crustal magmatic modification: lower crustal intrusions (i.e., extensive underplate complexes) thicken the boundary between relatively fast wavespeed mantle and slow wavespeed crust, suppressing the amplitude of P-to-S Moho conversions in receiver functions, particularly at high frequencies (e.g., *Ogden et al.*, 2019). Most stations in northwestern Zambia produce good quality results using high-frequency receiver functions (Figure 3A), with high ACE values (Figure 4A), indicating a relatively sharp Moho and a lack of lower crustal intrusions. Our results, interpreted in light of petrological studies (*Tembo et al.*, 1999; *Bacha et al.*, 2023) that find metagabbroic sill thickness rarely exceeds 200 m in northern Zambia, indicate rela-

tively low volumes of magmatism accompanied Katangan Basin development, and is unlikely to have involved the formation of an LIP analogous in scale to the 30 Ma–recent Ethiopian traps (e.g., *Stuart et al.*, 2006; *Rooney et al.*, 2012). The same is true for the Zambezi Basin, where low  $V_P/V_S$  ratios (<1.78) in our analysis preclude the presence of voluminous gabbroic lower crustal intrusions and are instead indicative of dominantly felsic bulk-crustal compositions.

Low  $V_P/V_S$  ratios also support the absence of ultramafic oceanic terranes, with the caveat that any oceanic lithosphere may have since completely subducted following the subsequent development of the Pan-African Orogeny. However, the Zambia-wide lack of evidence for arc-related magmatism from a subducting slab suggest the latter is an unlikely scenario (*Kampunzu and Cailteux*, 1999). Instead, geochemical characteristics of basaltic rocks near the Domes region match those produced in a continental rift environment that did not progress into sea-floor spreading (*Tembo et al.*, 1999; *Kampunzu and Cailteux*, 1999), corroborating our H- $\kappa$  stacking results.

Furthermore, receiver functions across the Katangan and Zambezi Basins generally lack the characteristic delay in the direct P-arrival typically seen in thick sedimentary basins worldwide (e.g., *Agrawal et al.*, 2022; *Maignier et al.*, 2024). This observation, when coupled with high ACE values (ACE>3) precludes the presence of a sharp velocity contrast between the older Paleoproterozoic basement and the base of the Katangan and Zambezi sedimentary sequences. This is unsurprising given the Neoproterozoic age of the Katangan and Zambezi Basins which have, at least in-part, been metamorphosed by the subsequent Pan-African Orogeny to form the Lufilian Arc and Zambezi Belt, respectively (e.g., *Porada and Berhorst*, 2000).

## 6.2 Crustal Structure Across the Central African Plateau: Implications for Crustal Shortening During the Pan-African Orogeny

Moho depth across the broad Central African Plateau generally ranges from 35 to 50 km. The crust is thickest at the Congo Craton margin (45–48 km), Domes region of the Lufilian Arc/Katangan Basin (46–48 km) and the Mesoproterozoic Irumide Belt (46–48 km), and thinnest in the Bangweulu Craton (38–42 km) and southeastern Zambia (35–40 km; Figure 3B).

The southeastern Congo Craton margin is defined by a gradual crustal thickness reduction of ~8 km into the Lufilian Arc/Katangan Basin — the thinnest point (~40 km) is thought to mark the westernmost extent of the Lufilian Arc/Katangan Basin (*Daly et al.*, 2024; *Rainaud et al.*, 2003). After its Neoproterozoic development, the Katangan Basin was overprinted by the Pan-African Orogeny in the early

Cambrian, giving rise to the Lufilian Arc. However, due to a lack of deep penetrating geophysical constraints, the extent and uniformity of crustal shortening across the region is uncertain. Our results reveal that the deepest and most highly variable Moho topography (38–48 km) across the entire region, lies below and adjacent to the Domes region (Zones II and III; Figures 1 and 5). Here, weak Moho conversions, lower CCC values (0.73–0.77), and relatively poor H- $\kappa$  stacking results (e.g., failure at station Z14M) potentially signify the presence of a complex, gradational Moho. Supporting this suggestion, ACE values are consistently lower (2–4; Figure 4A) than for adjacent CuBES stations to the north and south of the Domes region. Low  $V_P/V_S$  ratios (<1.8) likely rule out mafic underplating as a cause of the gradational Moho. Instead, the coincident exposure of Paleoproterozoic granitic basement and highest-grade regional metamorphism (e.g., *Porada and Berhorst, 2000; Cosi et al., 1992*), suggest the Domes region likely experienced the most intense crustal re-working/shortening during the Pan-African Orogeny. This is corroborated by the CuBES project shear-wave splitting analysis of *Kounoudis et al. (2024)*, who find that the largest variability in splitting parameters coincides with the Domes region, reflecting the lack of organised Lattice Preferred Orientation (LPO) fabric and the presence of depth-dependent anisotropy throughout the lithosphere.

In stark contrast, the Moho across the southern parts of the Lufilian Arc/Katangan Basin, and the remaining 450 km of the CuBES profile, is shallower and laterally consistent (~39 km; Figure 5). ACE values at these stations are consistently high (4–7; Figure 4A), indicating strong  $P_s$  conversions resulting from a sharp crust-mantle transition. The Katanga High (IV) portion of the Katangan Basin therefore appears to have experienced less re-working during the orogeny, an interpretation consistent with the low-grade metamorphic rocks present in these regions (e.g., *Porada and Berhorst, 2000; Naydenov et al., 2014*). Our H- $\kappa$  stacking results therefore corroborate the hypothesis of *Unrug (1983)* who suggested crustal shortening was larger at the western extremity of the Lufilian Arc. To explain a reduction of deformation in the southeast, as well as the Lufilian Arc's arcuate nature, *Unrug (1983)* further proposed the existence of a distinct and mechanically-resistant microplate in Zones III and IV (Figure 1A). Low bulk-crustal  $V_P/V_S$  ratios (<1.75) — indicative of Quartz-rich crust, which is relatively-weak (*Lowry and Pérez-Gussinyé, 2011*) — are consistent with those across the wider region (Figure 3C), suggesting a distinct, perhaps resistant, crustal block is unlikely to be located below the region. Furthermore, the relatively flat Moho topography, impulsive  $P_s$  Moho conversions and high ACE values at stations in this region, all indicate that distinct crustal blocks are unlikely to be present.

Despite all but one CuBES station passing the CCC criteria (CCC > 0.6), stations in Zone IV, have slightly below average CCC values compared to all stations in the CuBES network (Figure 4C). Upon

inspection of these receiver functions, including stations Z20L (Figure S18f) and Z22K (Figure S20f), there are significant intra-crustal arrivals in the 1–3 s time range. These arrivals, which vary depending on ray parameter and/or back azimuth, are the predominant cause of reduced CCC values in Zone IV, and are either a primary conversion from a mid-crustal velocity discontinuity, or reverberations from a shallower discontinuity.

In southern Zambia, the Choma-Kalomo Block has a crustal thickness (~37 km) and  $V_P/V_S$  ratio (~1.67–1.76) analogous to the Bangweulu Craton (Figure 3B). This is consistent with the view that the Block may be a re-worked fragment of cratonic crust (e.g., Glynn et al., 2017), not the southward continuation of the Irumide Belt, as assumed by some studies (e.g., Hanson et al., 1988; Kampunzu and Cailteux, 1999), which has a seemingly thicker crust (~48 km; Figure 3B). A crustal thickness of ~38 km is consistent with typical cratonic crust observed across the African continent (e.g., Kachingwe et al., 2015; Tugume et al., 2013; Durrheim and Mooney, 1994).

### 6.3 Crustal Structure Across Major Shear Zones and Suture Zones

Postdating the main phase of the Pan-African Orogeny (~560–550 Ma), is the development of several shear-zones (~520 Ma), most notably, the Mwembeshi Shear Zone in southeastern Zambia. The shear-zone is assumed to mark the main suture between the colliding Congo and Kalahari Cratons (e.g., Coward and Daly, 1984; John and Schenk, 2003), separating the low metamorphic-grade section of the Lufilian Arc from the higher-grade Zambezi Belt (Figure 1A). In our H- $\kappa$  stacking results, Moho depth (Figure 5), bulk crustal  $V_P/V_S$  (Figure 3C) and CCC (Figure 4C) are consistent across the shear-zone suggesting the crust either side of the shear-zone is structurally and compositionally similar. The Mwembeshi Shear Zone is thus unlikely to have developed at a zone of major crustal heterogeneity instigated by the juxtaposition of two completely distinct crustal domains. Instead, it may simply separate regions of similar thickness and crustal composition, or perhaps developed within a previously uniform terrane. Nevertheless, slightly less impulsive P-to-S Moho conversions in the receiver functions (ACE = 2–4; Figure 4A) are evident within the Zambezi Belt south of the Mwembeshi Shear Zone (Figure 5), signifying a minor difference in crustal domains. Weaker primary Moho conversions have been observed in remnant subduction zone settings worldwide (e.g., Frassetto et al., 2011; Gilligan et al., 2016; Ogden et al., 2019), and this could provide evidence that the Zambezi Belt was situated in a Neoproterozoic subduction zone setting.

## 7 Conclusions

We present new receiver function H- $\kappa$  stacking constraints on Moho depth and bulk-crustal  $V_P/V_S$  ratio below the Central African Plateau for a combined seismograph network of 70 stations, including the Copper Basin Exploration Science (CuBES) network deployed in 2022–2023 across central Zambia.

Our results reveal a ~10–13 km variation in Moho depth across the Plateau. The crust is thickest below the Congo Craton margin (45–48 km), the Mesoproterozoic Irumide belt (46–48 km), and the Domes region of the Lufilian Arc/Katangan Basin (46–48 km); thinner crust is found in the Bangweulu Craton (38–42 km), and the Zambezi Belt (35–40 km) in southeastern Zambia. Bulk-crustal  $V_P/V_S$  is generally low (<1.76) across the majority of the Plateau, indicating a dominantly felsic crustal composition that is consistent with the widespread presence of Quartz-rich granite. Mafic magmatism (dikes, sills and pillow lavas) has been mapped in various locations across the Neoproterozoic Katangan Basin, however in light of our low  $V_P/V_S$  results, the extent of crustal modification is relatively low compared to other major LIPs worldwide. The formation of the Katangan Basin is thus unlikely to have been accompanied by voluminous mafic lower crustal intrusions/thick magmatic underplate, and/or the formation of oceanic crust. The early-Paleozoic Pan-African orogenic overprinting of the Katangan Basin, forming the Lufilian Arc, appears to have been most intense in the Domes region, where a deep and highly variable (38–48 km) Moho topography at short length-scales (<100 km), is evident in our H- $\kappa$  stacking results. In contrast, Moho depth across the southern parts of the Katangan Basin/Lufilian Arc and Zambezi Belt are laterally consistent (~38 km) and therefore may have experienced reduced crustal shortening during the Pan-African Orogeny. Furthermore, crustal thickness and  $V_P/V_S$  ratio remain consistent across the Mwembeshi Shear Zone, suggesting it likely developed between, and/or juxtaposes, two very similar crustal domains.

### Declaration of Competing Interest

The authors declare that they have no known competing financial interests or personal relationships that could have appeared to influence the work reported in this paper.

### Data Availability Statement

The facilities of EarthScope Consortium were used for access to waveforms, related metadata, and/or derived products used in this study. These services are funded through the National Science Foun-

dation's Seismological Facility for the Advancement of Geoscience (SAGE) Award under Cooperative Agreement EAR-1724509. All seismic data were downloaded through the EarthScope Consortium Web Services (<https://service.iris.edu/>) for the following networks: the ZP ([Nyblade, 2007](#)), AF ([Penn State University, 2004](#)), BX ([Botswana Geoscience Institute, 2001](#)), XK ([Gao et al., 2012](#)) and IU ([Albuquerque Seismological Laboratory/USGS, 2014](#)) networks. Broadband seismograph data for CuBES stations will be available in November 2026 via EarthScope Consortium Web Services.

## Acknowledgements

We thank the SEIS-UK data management facility ([Brisbourne, 2012](#)) for providing seismograph instruments deployed across Zambia for the CuBES seismograph network and thank M. Chifita, T. Hudson, R. Kaluba, T. Mackay-Champion, M. Mutale, A. Ngulube and G. Shiyanga for their valuable fieldwork assistance during the installation and maintenance of the network. The sensors were provided by the NERC GEF, under loan 1110. We acknowledge collaboration with the Zambian Ministry of Mines and their help in establishing the CuBES seismograph network, as well as First Quantum Minerals (FQM) and Kalahari GeoEnergy for their logistical help during fieldwork. We also acknowledge support from the wider Basin Analysis and Multi-Physics on the Central African Copper Belt (CACB) group led by the Department of Earth Sciences at the University of Oxford. This work was supported by the Natural Environment Research Council "Copper Basin Exploration Science (CuBES)" project through grant numbers NE/T003766/1 and NE/T003170/1 awarded to the University of Leicester and Oxford University, respectively. For the purposes of open access, the author has applied a Creative Commons Attribution (CC BY) licence to any Author Accepted Manuscript (AAM) version arising from this submission.

## References

- Agrawal, S., C. M. Eakin, and J. O'Donnell (2022), Characterizing the cover across South Australia: a simple passive-seismic method for estimating sedimentary thickness, *Geophys. J. Int.*, 231(3), 1850–1864, doi:[10.1093/gji/ggac294](https://doi.org/10.1093/gji/ggac294).
- Albuquerque Seismological Laboratory/USGS (2014), Global Seismograph Network (GSN - IRIS/USGS) [Data set], doi:[10.7914/SN/IU](https://doi.org/10.7914/SN/IU).
- Bacha, R., J. Mungall, and R. Ernst (2023), Petrogenesis of the Katangan mafic rocks, Zambia: In-

sights from lithogeochemistry, large igneous province classification, and petrological modeling, *Results in Geochemistry*, 12, 100,027, doi:[10.1016/j.ringeo.2023.100027](https://doi.org/10.1016/j.ringeo.2023.100027).

Begg, G. C., W. L. Griffin, L. M. Natapov, S. Y. O'Reilly, S. P. Grand, C. J. O'Neill, J. M. A. Hronsky, Y. P. Djomani, C. J. Swain, T. Deen, et al. (2009), The lithospheric architecture of Africa: Seismic tomography, mantle petrology, and tectonic evolution, *Geosphere*, 5(1), 23–50, doi:[10.1130/GES00179.1](https://doi.org/10.1130/GES00179.1).

Botswana Geoscience Institute (2001), Botswana Seismological Network [Data set], doi:[10.7914/SN/BX](https://doi.org/10.7914/SN/BX).

Brisbourne, A. (2012), How to store and share geophysical data, *Astronomy and Geophysics*, 53(4), 19–20, doi:[10.1111/j.1468-4004.2012.53419.x](https://doi.org/10.1111/j.1468-4004.2012.53419.x).

Catuneanu, O., H. Wopfner, P. Eriksson, B. Cairncross, B. Rubidge, R. Smith, and P. Hancock (2005), The Karoo basins of south-central Africa, *J. Aeronaut. Sci.*, 43(1-3), 211–253, doi:[10.1016/j.jafrearsci.2005.07.007](https://doi.org/10.1016/j.jafrearsci.2005.07.007).

Chen, Y., Y. Xu, T. Xu, S. Si, X. Liang, X. Tian, Y. Deng, L. Chen, P. Wang, Y. Xu, et al. (2015), Magmatic underplating and crustal growth in the Emeishan Large Igneous Province, SW China, revealed by a passive seismic experiment, *Earth Planet. Sci. Lett.*, 432, 103–114, doi:[10.1016/j.epsl.2015.09.048](https://doi.org/10.1016/j.epsl.2015.09.048).

Christensen, N. I. (1996), Poisson's ratio and crustal seismology, *J. Geophys. Res. Solid Earth*, 101(B2), 3139–3156, doi:[10.1029/95JB03446](https://doi.org/10.1029/95JB03446).

Cosi, M., A. De Bonis, G. Gosso, J. Hunziker, G. Martinotti, S. Moratto, J. Robert, and F. Ruhlman (1992), Late Proterozoic thrust tectonics, high-pressure metamorphism and uranium mineralization in the Domes area, Lufilian Arc, northwestern Zambia, *Precambrian Research*, 58(1-4), 215–240, doi:[10.1016/0301-9268\(92\)90120-D](https://doi.org/10.1016/0301-9268(92)90120-D).

Coward, M., and M. Daly (1984), Crustal lineaments and shear zones in Africa: their relationship to plate movements, *Precambrian Research*, 24(1), 27–45, doi:[10.1016/0301-9268\(84\)90068-8](https://doi.org/10.1016/0301-9268(84)90068-8).

Daly, E., D. Keir, C. Ebinger, G. Stuart, I. Bastow, and A. Ayele (2008), Crustal tomographic imaging of a transitional continental rift: The Ethiopian rift, *Geophys. J. Int.*, 172(3), 1033–1048, doi:[10.1111/j.1365-246X.2007.03682.x](https://doi.org/10.1111/j.1365-246X.2007.03682.x).

Daly, M. (1986), The intracratonic Irumide belt of Zambia and its bearing on collision

orogeny during the Proterozoic of Africa, *Geol. Soc. Lond. Spec. Pub.*, 19(1), 321–328, doi:[10.1144/GSL.SP.1986.019.01.18](https://doi.org/10.1144/GSL.SP.1986.019.01.18).

Daly, M., P. Green, A. Watts, O. Davies, F. Chibesakunda, and R. Walker (2020), Tectonics and landscape of the Central African Plateau and their implications for a propagating Southwestern Rift in Africa, *Geochem. Geophys. Geosyst.*, 21(6), e2019GC008,746, doi:[10.1029/2019GC008746](https://doi.org/10.1029/2019GC008746).

Daly, M., M. Zimba, M. Purkiss, and F. Chibesakunda (2024), Lithospheric Thickness, Rift and Inversion Tectonics: The Formation and Deformation of the Neoproterozoic Katangan Basin of Central Africa, *In-review*.

Daly, M. C. (1988), Crustal shear zones in Central Africa: a kinematic approach to Proterozoic tectonics, *Episodes Journal of International Geoscience*, 11(1), 5–11, doi:[10.18814/epiugs/1988/v11i1/003](https://doi.org/10.18814/epiugs/1988/v11i1/003).

de Swardt, A. J., P. Garrard, and J. Simpson (1965), Major zones of transcurrent dislocation and superposition of orogenic belts in part of central Africa, *Geological Society of America Bulletin*, 76(1), 89–102, doi:[10.1130/0016-7606\(1965\)76\[89:MZOTDA\]2.0.CO;2](https://doi.org/10.1130/0016-7606(1965)76[89:MZOTDA]2.0.CO;2).

De Waele, B., and B. Mapani (2002), Geology and correlation of the central Irumide belt, *J. Aeronaut. Sci.*, 35(3), 385–397, doi:[10.1016/S0899-5362\(02\)00149-5](https://doi.org/10.1016/S0899-5362(02)00149-5).

Durrheim, R. J., and W. D. Mooney (1994), Evolution of the Precambrian lithosphere: seismological and geochemical constraints, *J. Geophys. Res. Solid Earth*, 99(B8), 15,359–15,374, doi:[10.1029/94JB00138](https://doi.org/10.1029/94JB00138).

Eglinger, A., O. Vanderhaeghe, A.-S. André-Mayer, P. Goncalves, A. Zeh, C. Durand, and E. Deloule (2016), Tectono-metamorphic evolution of the internal zone of the Pan-African Lufilian orogenic belt (Zambia): Implications for crustal reworking and syn-orogenic uranium mineralizations, *Lithos*, 240, 167–188, doi:[10.1016/j.lithos.2015.10.021](https://doi.org/10.1016/j.lithos.2015.10.021).

Fadel, I., M. van der Meijde, and H. Paulssen (2018), Crustal structure and dynamics of Botswana, *J. Geophys. Res. Solid Earth*, 123(12), 10–659, doi:[10.1029/2018JB016190](https://doi.org/10.1029/2018JB016190).

Frassetto, A., G. Zandt, H. Gilbert, T. Owens, and C. Jones (2011), Structure of the Sierra Nevada from receiver functions and implications for lithospheric foundering, *Geosphere*, 7(4), 898–921, doi:[10.1130/GES00570.1](https://doi.org/10.1130/GES00570.1).

- Fritz, H., M. Abdelsalam, K. A. Ali, B. Bingen, A. S. Collins, A. R. Fowler, W. Ghebreab, C. A. Hauzenberger, P. R. Johnson, T. M. Kusky, et al. (2013), Orogen styles in the East African Orogen: a review of the Neoproterozoic to Cambrian tectonic evolution, *J. Afr. Earth Sci.*, 86, 65–106, doi:[10.1016/j.jafrearsci.2013.06.004](https://doi.org/10.1016/j.jafrearsci.2013.06.004).
- Gao, S., K. Liu, M. Abdelsalam, and H. John (2012), Seismic Arrays for African Rift Initiation [Data set], doi:[10.7914/SN/XK\\_2012](https://doi.org/10.7914/SN/XK_2012).
- Gilligan, A., I. D. Bastow, and F. A. Darbyshire (2016), Seismological structure of the 1.8 Ga Trans-Hudson Orogen of North America, *Geochem. Geophys. Geosyst.*, 17(6), 2421–2433, doi:[10.1002/2016GC006419](https://doi.org/10.1002/2016GC006419).
- Glynn, S. M., S. Master, M. Wiedenbeck, D. W. Davis, J. D. Kramers, G. A. Belyanin, D. Frei, and T. Oberthür (2017), The Proterozoic Choma-Kalomo block, SE Zambia: Exotic terrane or a reworked segment of the Zimbabwe craton?, *Precambrian Research*, 298, 421–438, doi:[10.1016/j.precamres.2017.06.020](https://doi.org/10.1016/j.precamres.2017.06.020).
- Hanson, R. E., T. J. Wilson, and M. S. Wardlaw (1988), Deformed batholiths in the Pan-African Zambezi belt, Zambia: age and implications for regional Proterozoic tectonics, *Geology*, 16(12), 1134–1137, doi:[10.1130/0091-7613\(1988\)016<1134:DBITPA>2.3.CO;2](https://doi.org/10.1130/0091-7613(1988)016<1134:DBITPA>2.3.CO;2).
- Hanson, R. E., T. J. Wilson, and H. Munyanyiwa (1994), Geologic evolution of the Neoproterozoic Zambezi orogenic belt in Zambia, *J. Aeronaut. Sci.*, 18(2), 135–150, doi:[10.1016/0899-5362\(94\)90026-4](https://doi.org/10.1016/0899-5362(94)90026-4).
- Holwell, D. A., C. L. Mitchell, G. A. Howe, D. M. Evans, L. A. Ward, and R. Friedman (2017), The Munali Ni sulfide deposit, southern Zambia: A multi-stage, mafic-ultramafic, magmatic sulfide-magnetite-apatite-carbonate megabreccia, *Ore Geol. Rev.*, 90, 553–575, doi:[10.1016/j.oregeorev.2017.02.034](https://doi.org/10.1016/j.oregeorev.2017.02.034).
- John, T., and V. Schenk (2003), Partial eclogitisation of gabbroic rocks in a late Precambrian subduction zone (Zambia): prograde metamorphism triggered by fluid infiltration, *Contributions to Mineralogy and Petrology*, 146, 174–191, doi:[10.1007/s00410-003-0492-8](https://doi.org/10.1007/s00410-003-0492-8).
- Julia, J., C. J. Ammon, and A. A. Nyblade (2005), Evidence for mafic lower crust in Tanzania, East Africa, from joint inversion of receiver functions and Rayleigh wave dispersion velocities, *Geophys. J. Int.*, 162(2), 555–569, doi:[10.1111/j.1365-246X.2005.02685.x](https://doi.org/10.1111/j.1365-246X.2005.02685.x).

Kachingwe, M., A. Nyblade, and J. Julia (2015), Crustal structure of Precambrian terranes in the southern African subcontinent with implications for secular variation in crustal genesis, *Geophys. J. Int.*, 202(1), 533–547, doi:[10.1093/gji/ggv136](https://doi.org/10.1093/gji/ggv136).

Kampunzu, A., and J. Cailteux (1999), Tectonic Evolution of the Lufilian Arc (Central Africa Copper Belt) During Neoproterozoic Pan African Orogenesis, *Gondwana Research*, 2(3), 401–421, doi:[https://doi.org/10.1016/S1342-937X\(05\)70279-3](https://doi.org/10.1016/S1342-937X(05)70279-3).

Kounoudis, R., J. Kendall, C. Ogden, S. Fishwick, C. Chifwepa, and M. Daly (2024), The Tectonic Development of the Central African Plateau: Evidence from Shear-Wave Splitting, *Geophys. J. Int.*, p. ggae345, doi:[10.1093/gji/ggae345](https://doi.org/10.1093/gji/ggae345).

Langston, C. (1977), The Effect of Planar Dipping Structure on Source and Receiver Responses for Constant Ray Parameter, *Bull. Seis. Soc. Am.*, 67(4), 1029, doi:[10.1785/BSSA0670041029](https://doi.org/10.1785/BSSA0670041029).

Ligorria, J., and C. Ammon (1999), Iterative deconvolution and receiver-function estimation, *Bull. Seis. Soc. Am.*, 89(5), 1395–1400, doi:[10.1785/BSSA0890051395](https://doi.org/10.1785/BSSA0890051395).

Lowry, A. R., and M. Pérez-Gussinyé (2011), The role of crustal quartz in controlling Cordilleran deformation, *Nature*, 471(7338), 353–357, doi:[10.1038/nature09912](https://doi.org/10.1038/nature09912).

Mackenzie, G. D., P. K. H. Maguire, L. A. Coogan, M. A. Khan, M. Eaton, and G. Petrides (2006), Geophysical constraints on the crustal architecture of the Troodos ophiolite: results from the IANGASS project, *Geophys. J. Int.*, 167(3), 1385–1401, doi:[10.1111/j.1365-246X.2006.03144.x](https://doi.org/10.1111/j.1365-246X.2006.03144.x).

Marignier, A., C. M. Eakin, B. Hejrani, S. Agrawal, and R. Hassan (2024), Sediment thickness across Australia from passive seismic methods, *Geophys. J. Int.*, 237(2), 849–861, doi:[10.1093/gji/ggae070](https://doi.org/10.1093/gji/ggae070).

Naydenov, K. V., J. Lehmann, K. Saalmann, L. Milani, J. A. Kinnaird, G. Charlesworth, D. Frei, and W. Rankin (2014), New constraints on the Pan-African Orogeny in Central Zambia: A structural and geochronological study of the Hook Batholith and the Mwembeshi Zone, 637, 80–105, doi:[10.1016/j.tecto.2014.09.010](https://doi.org/10.1016/j.tecto.2014.09.010).

Nyblade, A. (2007), Africa Array- Uganda/Tanzania [Data Set], doi:[10.7914/sn/zp\\_2007](https://doi.org/10.7914/sn/zp_2007).

Ogden, C., I. Bastow, C. Ebinger, A. Ayele, R. Kounoudis, M. Musila, R. Bendick, N. Mariita, G. Kianji, T. Rooney, et al. (2023), The development of multiple phases of superposed rifting in the Turkana

- Depression, East Africa: Evidence from receiver functions, *Earth Planet. Sci. Lett.*, 609, 118,088, doi:[10.1016/j.epsl.2023.118088](https://doi.org/10.1016/j.epsl.2023.118088).
- Ogden, C. S., and I. D. Bastow (2022), The crustal structure of the Anatolian Plate from receiver functions and implications for the uplift of the central and eastern Anatolian plateaus, *Geophys. J. Int.*, 229(2), 1041–1062, doi:[10.1093/gji/ggab513](https://doi.org/10.1093/gji/ggab513).
- Ogden, C. S., I. D. Bastow, A. Gilligan, and S. Rondenay (2019), A reappraisal of the H- $\kappa$  stacking technique: implications for global crustal structure, *Geophys. J. Int.*, 219(3), 1491–1513, doi:[10.1093/gji/ggz364](https://doi.org/10.1093/gji/ggz364).
- Ogden, C. S., D. Keir, I. D. Bastow, A. Ayele, S. Marcou, F. Ugo, A. Woodward, B. A. Kibret, and S. Gudbrandsson (2021), Seismicity and crustal structure of the southern Main Ethiopian Rift: New evidence from Lake Abaya, *Geochem. Geophys. Geosyst.*, 22(8), e2021GC009,831, doi:[10.1029/2021GC009831](https://doi.org/10.1029/2021GC009831).
- Paparrizos, J., and L. Gravano (2015), k-shape: Efficient and accurate clustering of time series, in *Proceedings of the 2015 ACM SIGMOD international conference on management of data*, pp. 1855–1870, doi:[10.1145/2723372.2737793](https://doi.org/10.1145/2723372.2737793).
- Penn State University (2004), AfricaArray [Data set], doi:[10.7914/SN/AF](https://doi.org/10.7914/SN/AF).
- Phinney, R. A. (1964), Structure of Earths crust from spectral behavior of long-period body waves, *J. Geophys. Res.*, 69, 2997–3017, doi:[10.1002/2016JB013599](https://doi.org/10.1002/2016JB013599).
- Porada, H. (1989), Pan-African rifting and orogenesis in southern to equatorial Africa and eastern Brazil, *Precambrian Research*, 44(2), 103–136, doi:[10.1016/0301-9268\(89\)90078-8](https://doi.org/10.1016/0301-9268(89)90078-8).
- Porada, H., and V. Berhorst (2000), Towards a new understanding of the Neoproterozoic-Early Palaeozoic Lufilian and northern Zambezi Belts in Zambia and the Democratic Republic of Congo, *J. Aeronaut. Sci.*, 30(3), 727–771, doi:[10.1016/S0899-5362\(00\)00049-X](https://doi.org/10.1016/S0899-5362(00)00049-X).
- Rainaud, C., S. Master, R. Armstrong, and L. Robb (2003), A cryptic Mesoarchaean terrane in the basement to the Central African Copperbelt, *J. Geol. Soc.*, 160(1), 11–14, doi:[10.1144/0016-764902-087](https://doi.org/10.1144/0016-764902-087).
- Reddy, P., and V. V. Rao (2013), Seismic images of the continental Moho of the Indian shield, 609, 217–233, doi:[10.1016/j.tecto.2012.11.022](https://doi.org/10.1016/j.tecto.2012.11.022).

- Rooney, T. O., C. Herzberg, and I. D. Bastow (2012), Elevated mantle temperature beneath East Africa, *Geology*, 40(1), 27–30, doi:[10.1130/G32382.1](https://doi.org/10.1130/G32382.1).
- Sarafian, E., R. L. Evans, M. G. Abdelsalam, E. Atekwana, J. Elsenbeck, A. G. Jones, and E. Chikambwe (2018), Imaging Precambrian lithospheric structure in Zambia using electromagnetic methods, *Gondwana Research*, 54, 38–49, doi:[10.1016/j.gr.2017.09.007](https://doi.org/10.1016/j.gr.2017.09.007).
- Schimmel, M., and H. Paulssen (1997), Noise reduction and detection of weak, coherent signal through phase-weighted stacks, *Geophys. J. Int.*, 130, 497–505, doi:[10.1111/j.1365-246X.1997.tb05664.x](https://doi.org/10.1111/j.1365-246X.1997.tb05664.x).
- Stuart, G. W., I. D. Bastow, and C. J. Ebinger (2006), Crustal structure of the northern Main Ethiopian Rift from receiver function studies, *Geol. Soc. Lond. Spec. Pub.*, 259(1), 253–267, doi:[10.1144/GSL.SP.2006.259.01.20](https://doi.org/10.1144/GSL.SP.2006.259.01.20).
- Sun, M., S. S. Gao, K. H. Liu, K. Mickus, X. Fu, and Y. Yu (2021), Receiver function investigation of crustal structure in the malawi and luangwa rift zones and adjacent areas, *Gondwana Research*, 89, 168–176, doi:[10.1016/j.gr.2020.08.015](https://doi.org/10.1016/j.gr.2020.08.015).
- Tavenard, R., J. Faouzi, G. Vandewiele, F. Divo, G. Androz, C. Holtz, M. Payne, R. Yurchak, M. Rußwurm, K. Kolar, and E. Woods (2020), Tslearn, A Machine Learning Toolkit for Time Series Data, *J. Mach. Learn. Res.*, 21(118), 1–6, doi:[jmlr.org/papers/v21/20-091.html](https://jmlr.org/papers/v21/20-091.html).
- Tembo, F., A. Kampunzu, and H. Porada (1999), Tholeiitic magmatism associated with continental rifting in the Lufilian Fold Belt of Zambia, *J. Aeronaut. Sci.*, 28(2), 403–425, doi:[10.1016/S0899-5362\(99\)00012-3](https://doi.org/10.1016/S0899-5362(99)00012-3).
- Thieme, J. G., and R. L. Johnson (1981), The Geological Map of the Republic of Zambia, 1:1,000,000., *Geological Survey Department, Ministry of Mines, Lusaka, Zambia*.
- Thompson, D., I. Bastow, G. Helffrich, J.-M. Kendall, J. Wookey, D. Snyder, and D. Eaton (2010), Precambrian crustal evolution: Seismic constraints from the Canadian Shield, *Earth Planet. Sci. Lett.*, 297, 655–666, doi:[10.1016/j.epsl.2010.07.021](https://doi.org/10.1016/j.epsl.2010.07.021).
- Tugume, F., A. Nyblade, J. Julià, and M. van der Meijde (2013), Precambrian crustal structure in Africa and Arabia: evidence lacking for secular variation, 609, 250–266, doi:[10.1016/j.tecto.2013.04.027](https://doi.org/10.1016/j.tecto.2013.04.027).
- Unrug, R. (1983), The Lufilian Arc: a microplate in the Pan-African collision zone of the Congo and the Kalahari cratons, *Precambrian Research*, 21(3-4), 181–196, doi:[10.1016/0301-9268\(83\)90040-2](https://doi.org/10.1016/0301-9268(83)90040-2).

Wang, T., J. Feng, K. H. Liu, and S. S. Gao (2019), Crustal structure beneath the Malawi and Luangwa Rift Zones and adjacent areas from ambient noise tomography, *Gondwana Research*, 67, 187–198, doi:[10.1016/j.gr.2018.10.018](https://doi.org/10.1016/j.gr.2018.10.018).

Wedmore, L. N., T. Turner, J. Biggs, J. N. Williams, H. M. Sichingabula, C. Kabumbu, and K. Banda (2022), The Luangwa Rift Active Fault Database and fault reactivation along the southwestern branch of the East African Rift, *Solid Earth*, 13(11), 1731–1753, doi:[10.5194/se-13-1731-2022](https://doi.org/10.5194/se-13-1731-2022).

Xu, K.-k., W. Xie, K. Sun, J.-p. Ren, P.-h. Gong, S.-f. He, Y.-g. Lu, and H. Zhang (2022), Geochronology, geochemistry, and petrogenesis of I-and A-type granites in the Solwezi Dome of the Lufilian Arc: implications for the late-Mesoproterozoic magmatic and geodynamic evolution in northern Zambia, *Arabian Journal of Geosciences*, 15(23), 1729, doi:[10.1007/s12517-022-10971-0](https://doi.org/10.1007/s12517-022-10971-0).

Zhu, L., and H. Kanamori (2000), Moho depth variation in southern California from teleseismic receiver functions, *J. Geophys. Res.*, 105(B2), 2969–2980, doi:[10.1016/S0012-821X\(00\)00101-1](https://doi.org/10.1016/S0012-821X(00)00101-1).